Smart Materials and Structures

PAPER

Modeling thermal and buckling behavior in electrothermal bimorphs

To cite this article: Hussein Hussein *et al* 2024 *Smart Mater. Struct.* **33** 125042

IOP Publishing Smart Materials and Structures
Smart Mater. Struct. **33** (2024) 125042 (14pp) https://doi.org/10.1088/1361-665X/ad9445

Modeling thermal and buckling behavior in electrothermal bimorphs

Hussein Hussein[1,*], Quentin A A Tanguy[2], Issam Lakkis[1], Hossein Fariborzi[3], Arka Majumdar[2,4] and Karl F Böhringer[2,5]

[1] Department of Mechanical Engineering, MSFEA, American University of Beirut, Beirut 1107 2020, Lebanon
[2] Department of Electrical & Computer Engineering, University of Washington, Seattle 98195, WA, United States of America
[3] King Abdullah University of Science and Technology, Thuwal 23955-6900, Saudi Arabia
[4] Department of Bioengineering, University of Washington, Seattle 98195, WA, United States of America
[5] Department of Physics, University of Washington, Seattle 98195, WA, United States of America

E-mail: hh224@aub.edu.lb

Received 2 September 2024, revised 31 October 2024
Accepted for publication 18 November 2024
Published 29 November 2024

Abstract

Buckling is a structural phenomenon that can induce significant motion with minimal input variation. Electrothermal bimorphs, with their simple input and compact design, can leverage out-of-plane buckling motion for a broad range of applications. This paper presents the development of analytical electrothermal and structural models for such bimorphs. The electrothermal model calculates the temperature distribution within the bimorph caused by electrothermal heating, providing a 2D explicit analytical expression for estimating temperature along the bimorph's length and cross-section. Nonhomogeneous heating leads to varying strains, which induce axial forces and moments along the bimorph's neutral plane, varying with thermal expansion. The structural model derives the governing equation of deformation for the bimorph by analyzing internal strains and stresses resulting from deformation, electrothermal heating, and residual stresses. An analytical solution for deflection is obtained, incorporating infinite sums of heating and buckling modes, with closed-form equivalent expressions when possible. The bimorph's behavior under different scenarios of residual stresses and electrothermal heating is elucidated based on the analytical model. Comparisons with finite element simulations demonstrated excellent agreement, highlighting the high accuracy of the proposed models.

Keywords: buckling, electrothermal bimorph, modeling, MEMS

1. Introduction

With the growing demand for tunability in photonic devices [1–3], micro-electro-mechanical systems (MEMS) technology holds an unequivocal candidacy as it can offer repeatability and extensive continuous tunability ranges [4–9]. Electrothermal actuation, in particular, is mainly appreciated for its large range of motion and low actuation voltage [10–12]. Micro cantilevers and buckling beams are essential components of MEMS actuators, utilized in various applications due to their distinct mechanical properties. Unlike cantilevers, buckling beams enable compact design tip-tilt free motions or bistability, which is beneficial in multiple applications [13]. They have been deployed in bistable switches [14–16], energy harvesting devices [17], micropositioning devices [18, 19], microbots [20, 21] and as optical tuning elements [22], among others.

Buckling of beams has been studied since the 18th century, grounded in Euler's equations, which describe the unpredictable direction of deflection beyond the critical buckling

* Author to whom any correspondence should be addressed.

load. Extensive modeling studies have addressed the buckling of single-material structures [23–25]. The buckling of multi-layer bimorphs has been mainly investigated in the context of piezoelectric actuation [26, 27]. While electrothermal actuation of bimorph cantilevers has been analyzed [28], there is, to our knowledge, no analytical model for electrothermally-induced buckling of bimorph beams.

Modeling the buckling of electrothermal bimorphs requires an integrated approach that combines an electrothermal model, mapping electrical power to structural heating, with a structural model, translating thermal expansion to bimorph buckling. Existing electrothermal models are typically one-dimensional and based on the heat-transport equation [29–31] and lumped-element models for conduction [32]. Advanced approaches by Todd *et al* describe the electrothermal and structural behaviors of bimorph cantilever beams using lumped-element models [33, 34]. However, the structure of the bimorph necessitates a two-dimensional model to accurately calculate temperature distribution along the bimorph's length and across its layers.

This paper presents comprehensive analytical models for both the electrothermal and structural analysis of bimorph beams. The electrothermal model, developed in section 2, provides a two-dimensional explicit analytical expression to estimate temperature distribution along the bimorph's length and cross-section. This approach addresses nonhomogeneous heating, which results in varying strains and induces axial forces and moments along the bimorph's neutral plane, influenced by thermal expansion. Residual stresses from the fabrication process are considered in the modeling as those stresses are identified as a significant factor contributing to failures in experimental trials.

The structural model, developed in section 3, derives the governing equation for the bimorph deflection by analyzing internal strains and stresses resulting from deformation, heating, and residual stresses. An analytical solution for deflection is achieved, incorporating infinite sums of heating and buckling modes, with closed-form equivalent expressions where feasible. The behavior of the bimorph under various scenarios of residual stresses and electrothermal heating is discussed in section 4. The comparison in section 5 demonstrates strong agreement between the proposed models with finite element (FE) simulations in ANSYS, across various potential scenarios, confirming the accuracy of the proposed models.

2. Electrothermal model

A bimorph consists of a stack of two layers with different materials. Figure 1 shows a schematic of a bimorph with the different dimensions. The first material on top, has a Young's modulus E_1, a resistivity ρ_1, and a thermal expansion coefficient α_1. The second material at the bottom has a Young's modulus E_2, a resistivity ρ_2, and a thermal expansion coefficient α_2. The bimorph has a length l, a width b, and a thickness $t = t_1 + t_2$ with t_1 and t_2 being the thicknesses of the top and bottom layers, respectively. A_1 and A_2 depict the cross-section areas of both layers, respectively.

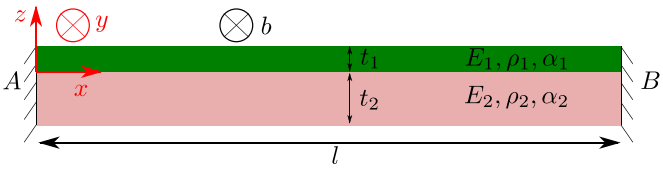

Figure 1. Diagram of leg components inputs and outputs.

The bimorph in figure 1 is fabricated in the xy plane and its deflection occurs along the out-of-plane z direction. The electrical voltage is applied between the bimorph's boundaries A and B. The electrical power flowing through the bimorph stack induced a buckling via Joule heating. The origin of the x axis is at point A and the origin of the y axis is at the intersection between both materials.

The convection and radiation are neglected in the model and the heat transfer is limited to the conduction. Thus, the temperature is considered homogeneous along the y direction. In contrast, the temperature is not homogeneous in the z direction as the bimorph consists of a stack of materials with different properties. The electrothermal modeling problem can be thus limited to the x and z directions. With these assumptions,the heat equation is expressed as follows [35]:

$$J_i^2 \rho_i + K_i \left(\frac{\partial^2 T}{\partial x^2} + \frac{\partial^2 T}{\partial z^2} \right) = 0 \tag{1}$$

where T is the temperature and J is the current density and K is the thermal conductivity. The index i refers to the material, $i = 1$ for the top material and $i = 2$ for the bottom material. For all the equations in the rest of the paper, i is set equal to 1 for $z \in [0, t_1]$ and equal to 2 for $z \in [-t_2, 0]$.

In the heat equilibrium equation, the rate of heat entering due to electrothermal heating minus the rate of heat leaving due to conduction equals the rate of temperature change, which becomes zero in the steady state. Using the steady-state equation in (1) for modeling is appropriate for quasistatic applications where the required dynamic behavior is slow compared to the response time of the electrothermal heating process. The heat equation (1) is solved using the separation of variables method:

$$T(x,z) = X(x)\,Z(z)\,. \tag{2}$$

The solution form for the temperature is obtained by introducing (2) into (1) and separating the variables.

$$\begin{aligned} T(x,z) = {} & c_1 x^2 + c_2 x + c_3 + c_4 z^2 + c_5 z + c_6 xz \\ & + (c_7 \cosh c_{11} x + c_8 \sinh c_{11} x) \\ & \times (c_9 \cos c_{11} z + c_{10} \sin c_{11} z) \\ & + (c_{12} \cos c_{16} x + c_{13} \sin c_{16} x) \\ & \times (c_{14} \cosh c_{16} z + c_{15} \sinh c_{16} z) \end{aligned} \tag{3}$$

where c_1 to c_{16} are constants that are determined depending on the boundary and continuity conditions.

Introducing (3) into (1) and considering $T = T_0$ at the bimorph ends connected to external support (Boundary sides

A and B in figure 1), the solution form reduces to the following form where constants c_4 to c_{12} are neglected and constants c_{13} to c_{16} have periodic solutions:

$$\begin{aligned} T(x,z)-T_0 = {} & \frac{\Delta v^2}{2K_i\rho_i l^2}\left(-x^2+lx\right) \\ & +\gamma\sum_{n=1}^{\infty}\frac{1}{n^3\pi^3}\sin\frac{n\pi x}{l} \\ & \times\left(a_{\text{in}}\cosh\frac{n\pi z}{l}+b_{\text{in}}\sinh\frac{n\pi z}{l}\right) \end{aligned} \tag{4}$$

where $\Delta v = l\rho_i J_i$ is the potential difference applied on the bimorph boundaries A and B. a_{in} and b_{in} are constants related the n^{th} periodic solution in (4). Note that if the product of the electrical resistivity and thermal conductivity ρK is equal or nearly equal for both materials, γ, which is a constant multiplied by the heating modes, will vanish. Consequently, the temperature will be uniform across the cross-section of the bimorph and will follow a parabolic distribution along its length. The heat transfer between both materials of the bimorph should conserve the continuity in temperature and in flow. In addition, the temperature flow at the lateral boundaries is neglected as the convection and radiation are negligible. These boundary and continuity conditions are expressed as:

$$\begin{cases} \dfrac{\mathrm{d}T}{\mathrm{d}z}(x,t_1)=0 \\ \dfrac{\mathrm{d}T}{\mathrm{d}z}(x,-t_2)=0 \\ T(x,0)_{i=1}=T(x,0)_{i=2} \\ -k_1\dfrac{\mathrm{d}T}{\mathrm{d}z}(x,0)_{i=1}=-k_2\dfrac{\mathrm{d}T}{\mathrm{d}z}(x,0)_{i=2}. \end{cases} \tag{5}$$

The constants a_{in} and b_{in}, $n=1,2,3,\ldots$, are calculated to satisfy the boundary and continuity conditions (5). Multiplying (5) by $\sin(n\pi x/l)$ and integrating it over the beam length helps to separate the n^{th} periodic constants a_{in} and b_{in} in the boundary and continuity conditions.

$$\begin{cases} \displaystyle\int_0^l \frac{\mathrm{d}T}{\mathrm{d}z}(x,t_1)\sin\frac{n\pi x}{l}\mathrm{d}x=0 \\ \displaystyle\int_0^l \frac{\mathrm{d}T}{\mathrm{d}z}(x,-t_2)\sin\frac{n\pi x}{l}\mathrm{d}x=0 \\ \displaystyle\int_0^l T(x,0)_{i=1}\sin\frac{n\pi x}{l}\mathrm{d}x \\ \qquad\displaystyle=\int_0^l T(x,0)_{i=2}\sin\frac{n\pi x}{l}\mathrm{d}x \\ \displaystyle\int_0^l -k_1\frac{\mathrm{d}T}{\mathrm{d}z}(x,0)_{i=1}\sin\frac{n\pi x}{l}\mathrm{d}x \\ \qquad\displaystyle=\int_0^l -k_2\frac{\mathrm{d}T}{\mathrm{d}z}(x,0)_{i=2}\sin\frac{n\pi x}{l}\mathrm{d}x. \end{cases} \tag{6}$$

The integrals in (6) neglect all the constants a_{ij} and b_{ij} with $j\neq n$. Thereby, a_{in} and b_{in} expressions are obtained by solving the linear equation system in (6). For the non-symmetrical solution modes $n=2,4,6,\ldots$, a_{in} and b_{in} are equal to zero.

$$\begin{cases} a_{1n}=b_{1n}=a_{2n}=b_{2n}=0 \\ n=2,4,6,\ldots. \end{cases} \tag{7}$$

For the symmetrical solution modes $n=1,3,5,\ldots$, a_{in} and b_{in} are expressed as:

$$\begin{cases} \gamma = 4\dfrac{\rho_2K_2-\rho_1K_1}{\rho_1\rho_2}\Delta v^2 \\ a_{1n}=-\dfrac{1}{\beta_nK_1}\cosh\dfrac{n\pi t_1}{l}\sinh\dfrac{n\pi t_2}{l} \\ b_{1n}=\dfrac{1}{\beta_nK_1}\sinh\dfrac{n\pi t_1}{l}\sinh\dfrac{n\pi t_2}{l} \\ a_{2n}=\dfrac{1}{\beta_nK_2}\sinh\dfrac{n\pi t_1}{l}\cosh\dfrac{n\pi t_2}{l} \\ b_{2n}=\dfrac{1}{\beta_nK_2}\sinh\dfrac{n\pi t_1}{l}\sinh\dfrac{n\pi t_2}{l} \\ \beta_n = K_1\sinh\dfrac{n\pi t_1}{l}\cosh\dfrac{n\pi t_2}{l} \\ \qquad +K_2\sinh\dfrac{n\pi t_2}{l}\cosh\dfrac{n\pi t_1}{l} \\ n=1,3,5,\ldots. \end{cases} \tag{8}$$

The temperature distribution in the electrothermal bimorph is calculated from (4) after considering the constants a_{in} and b_{in} calculated from (7) and (8). As the constants a_{in} and b_{in} are inversely proportional to n^3, a limited number of periodic solutions is sufficient to accurately estimate the temperature.

3. Structural model

3.1. Strain and stress distribution

Strains and stresses are induced in the longitudinal direction of the bimorph from four different sources: residual stress due to fabrication, axial strain due to the length compression between the two anchors, heating strain due to electrothermal heating, and bending strain due to the bending of the bimorph structure. Figure 2 shows a cross-section of the bimorph under deformation and the distribution of stress due to all sources.

3.1.1. Residual strain. Residual stress in an elastic body persists even without external force. In a multilayer micromachined bimorph, the distribution of residual stresses can be influenced by various factors, including material properties, fabrication processes, and thermal treatments. The residual stresses may not necessarily have the same level of stress or strain across different layers and may vary across the structure of each layer [36].

The design and fabrication processes of bimorphs may be tailored to achieve specific mechanical or thermal properties [37], involving adjustments to material properties, deposition control, or additional layers for stress distribution modification. In thin layers (< a few micrometers), completely avoiding residual stress growth is challenging and its effect

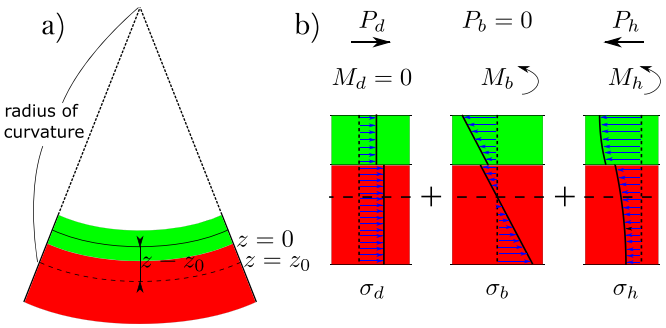

Figure 2. (a) Bending of a cross section of the bimorph. (b) Stresses, forces, and moments induced due to the length deformation, bending, and heating strains.

is non-negligible. This paper assumes a uniform residual strain for simplicity, justified by strain uniformity at the bimorph layer intersection and assuming relatively small thickness [36].

$$\varepsilon_r(x,z) = \varepsilon_r. \tag{9}$$

3.1.2. Axial strain. Once the bimorph is under deformation, the bimorph length is either compressed or expanded. A length deformation strain ε_{d} is induced in the bimorph in the axial direction. The expression of ε_d is shown in (10) with a simplified approximation considering small deformation hypothesis. ε_{d} is related to $w(x)$, which is the lateral deformation of the bimorph neutral plane along the x axis.

$$\varepsilon_{\mathrm{d}} = \sqrt{1+\left(\frac{\mathrm{d}w}{\mathrm{d}x}\right)^2} - 1 \approx \frac{1}{2}\left(\frac{\mathrm{d}w}{\mathrm{d}x}\right)^2. \tag{10}$$

3.1.3. Heating strain. The bimorph length expands due to electrothermal heating. This induces a length expansion that varies along z direction as the heating rate is not homogeneous between the two materials. The axial heat strain induced due to heating is calculated as follows:

$$\varepsilon_h(x,z) = \alpha_i\left(T(x,z) - T_0\right). \tag{11}$$

3.1.4. Bending strain. The bending strain ε_b is induced due to the local curvature of the bimorph structure after deformation. ε_b is calculated as follows:

$$\varepsilon_b(x,z) = \frac{z-z_0}{r(x)} \approx (z-z_0)\frac{\mathrm{d}^2 w}{\mathrm{d}x^2} \tag{12}$$

where $r(x)$ is the radius of curvature along the x direction and z_0 is the z level of the neutral plane. The bending stress is equivalently distributed relatively to the neutral plane. This characteristic helps to evaluate z_0.

$$\int_{-t_2}^{t_1} E_i\varepsilon_b \mathrm{d}z = 0 \longleftrightarrow z_0 = \frac{1}{2}\frac{E_1t_1^2 - E_2t_2^2}{E_1t_1 + E_2t_2}. \tag{13}$$

3.1.5. Total Strain. The total axial strain inside the bimorph is then the sum of the four strain components. Note that the axial strain is induced as elastic reaction for axial deformation and thus it induces strains opposite to the deformation direction.

$$\varepsilon_x(x,z) = \varepsilon_r - \varepsilon_d(x) + \varepsilon_h(x,z) + \varepsilon_b(x,z). \tag{14}$$

3.2. Axial force

The strains induced in the bimorph (14) result in an axial force P and moment $M(x)$ applied along the beam length. The axial force is induced as reaction forces are oppositely applied by the fixed bimorph ends due to the bimorph length expansion. Thus, as expansion in the bimorph's length leads to compression forces, in this paper we consider a positive sign for the axial strains in the case of expansion, and for the axial force and stresses in the case of compression. The axial force is equivalently distributed along the beam length and consists of one component related to the length deformation and another component related to the heating expansion. The bending strain has no effect on the axial force.

$$P = \frac{1}{l}\int_0^l\int_0^b\int_{-t_2}^{t_1} E_i\varepsilon_x \mathrm{d}z\mathrm{d}y\mathrm{d}x = P_r + P_d + P_h. \tag{15}$$

3.2.1. Residual strain force. The residual strain force P_r is evaluated from (15) considering (9):

$$P_r = R_a\varepsilon_r \tag{16}$$

where $R_a = E_1A_1 + E_2A_2$ is the axial rigidity for the bimorph. $A_1 = bt_1$ and $A_2 = bt_2$ are the bimorph cross-section areas for the first and second material layers, respectively.

3.2.2. Length expansion force. The length compression force P_d is evaluated from (10), (14), and (15):

$$P_d = -\frac{R_a}{2l}\int_0^l \left(\frac{\mathrm{d}w}{\mathrm{d}x}\right)^2 \mathrm{d}x. \tag{17}$$

3.2.3. Heating force. The heating force P_{h} is dependent on the temperature distribution calculated in the electrothermal model (4). P_{h} is evaluated considering (4), (11), (14), and (15):

$$\begin{aligned} P_{\mathrm{h}} = &\frac{\Delta v^2}{12}\left(\frac{E_1A_1\alpha_1}{K_1\rho_1} + \frac{E_2A_2\alpha_2}{K_2\rho_2}\right) \\ &+ 2bl\gamma\sum_{n=1,3,5,\ldots}\frac{E_2\alpha_2b_{2n} - E_1\alpha_1b_{1n}}{n^5\pi^5}. \end{aligned} \tag{18}$$

3.3. Moment on the neutral plane

The moment on the neutral plane due to the strains in (14) is calculated as follows:

$$M(x) = \int_0^b\int_{-t_2}^{t_1} E_i\varepsilon_x(z-z_0)\,\mathrm{d}z\mathrm{d}y = M_b(x) + M_h(x). \tag{19}$$

The residual and axial stresses are equally distributed between the two sides of the neutral plane, and thus their resulting moment in the cross section is zero.

3.3.1. Bending moment. The bending moment is calculated from (12), (14), and (19):

$$M_b(x) = R_f \frac{\mathrm{d}^2 w}{\mathrm{d}x^2} \tag{20}$$

where $R_f = E_1 I_1 + E_2 I_2$ is the flexural rigidity for the bimorph. I_1 and I_2 are the second quadratic moment for the first and second material layers, respectively:

$$\begin{cases} I_1 = b\left(\frac{1}{3}t_1^3 - t_1^2 z_0 + t_1 z_0^2\right) \\ I_2 = b\left(\frac{1}{3}t_2^3 + t_2^2 z_0 + t_2 z_0^2\right). \end{cases} \tag{21}$$

3.3.2. Heating moment. The shift between the center of heating strains in the cross-section and neutral plane results in a varying heating moment applied on neutral plane. The heating moment is calculated from (4), (11), (14), and (19):

$$M_h(x) = m\frac{-x^2 + lx}{l^2} + \sum_{n=1,3,5,\ldots} m_n \sin\frac{n\pi x}{l} \tag{22}$$

where the constants m and m_n are expressed as follows:

$$\begin{cases} m = \dfrac{bt_1 t_2 (t_1 + t_2)(\alpha_1 K_2 \rho_2 - \alpha_2 K_1 \rho_1) E_1 E_2 \Delta v^2}{4 K_1 K_2 \rho_1 \rho_2 (E_1 t_1 + E_2 t_2)} \\ m_n = \dfrac{blz_0\gamma}{n^4\pi^4}(E_1\alpha_1 b_{1n} - E_2\alpha_2 b_{2n}) \\ \qquad - \dfrac{bl^2\gamma}{n^5\pi^5}(E_1\alpha_1 m_{1n} + E_2\alpha_2 m_{2n}) \\ m_{1n} = \dfrac{1}{\beta_n K_1}\left(\cosh\dfrac{n\pi t_1}{l} - 1\right)\sinh\dfrac{n\pi t_2}{l} \\ m_{2n} = \dfrac{1}{\beta_n K_2}\left(\cosh\dfrac{n\pi t_2}{l} - 1\right)\sinh\dfrac{n\pi t_1}{l}. \end{cases} \tag{23}$$

The heating moment expression can be reformulated based on Fourier series along the beam length. This reformulation helps to extract solutions that are satisfying the boundary conditions in the structural model.

$$M_h(x) = c_{m0} + \sum_{i=1}^{\infty} c_{mi} \cos\frac{2i\pi x}{l} \tag{24}$$

where the constants c_{m0} and c_{mi} are calculated as follows:

$$\begin{cases} c_{m0} = \dfrac{1}{l}\displaystyle\int_0^l M_h(x)\,\mathrm{d}x = \frac{m}{6} + \sum_{n=1,3,5,\ldots} \frac{2m_n}{n\pi} \\ c_{mi} = \dfrac{2}{l}\displaystyle\int_0^l M_h(x)\cos\frac{2i\pi x}{l}\mathrm{d}x \\ \qquad = -\dfrac{m}{i^2\pi^2} - \displaystyle\sum_{n=1,3,5,\ldots} \frac{4m_n n}{(4i^2 - n^2)\pi}. \end{cases} \tag{25}$$

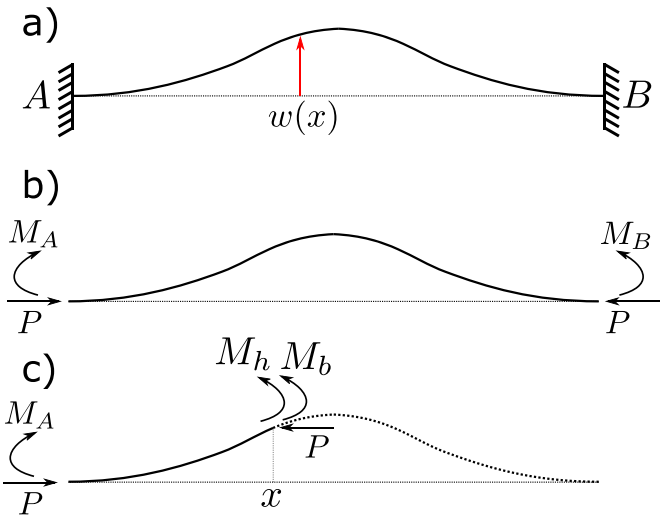

Figure 3. (a) Elastic Profile of the the bimorph after deflection. (b) Boundary reactions applied on the bimorph. (c) Boundary and internal reactions applied on a section of the bimorph.

Note that, as $M_h(x)$ is symmetric with respect to the bimorph mid-length ($x = l/2$), the Fourier series components multiplied by ($\sin 2i\pi x/l$) vanish in the calculation and are not shown in (25).

3.4. Governing equation and Normalization

Analyzing the force and moment diagram in figure 3, the Moment equilibrium equation is expressed as:

$$M_b(x) + M_h(x) + Pw(x) = M_A. \tag{26}$$

Deriving (26) two times relatively to x, the equilibrium equation is re-expressed as follows:

$$\frac{\mathrm{d}^4 W}{\mathrm{d}X^4} + N^2\frac{\mathrm{d}^2 W}{\mathrm{d}X^2} + \sum_{j=1,3,5,\ldots} \kappa_j \cos N_j X = 0 \tag{27}$$

where X, N, and κ_j are normalized parameters:

$$\begin{cases} X = \dfrac{x}{l}; \quad W(X) = w(x); \quad N = \sqrt{\dfrac{Pl^2}{R_f}} \\ N_j = (j+1)\pi \qquad j = 1,3,5,\ldots \\ \kappa_j = \dfrac{4l^2}{R_f}\left(m + \displaystyle\sum_{n=1,3,5,\ldots} \frac{n\pi N_j^2}{N_j^2 - n^2\pi^2} m_n\right). \end{cases} \tag{28}$$

3.5. Solution

The boundary conditions dictate that the shape of the bimorph after deformation can only take on certain periodic forms known as buckling modes. Consequently, the solution to the structural problem in (27) is an infinite sum of these buckling modes [12, 23–25].

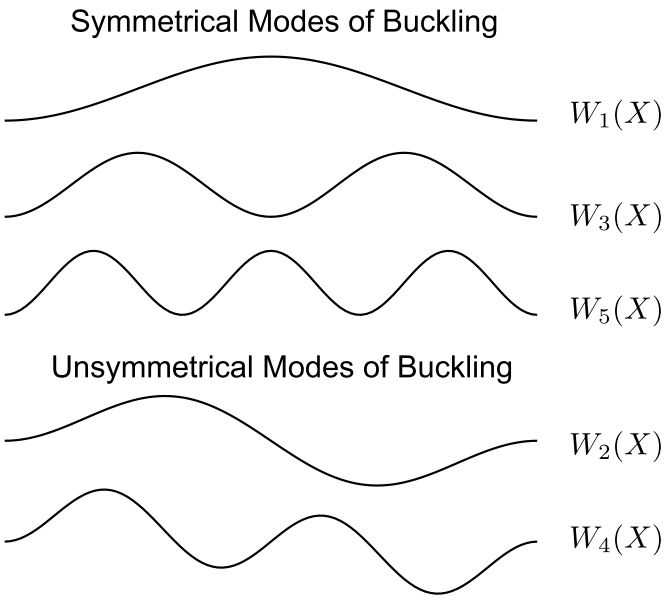

Figure 4. Shapes for the first five modes of buckling.

$$W(X)=\sum_{j=1}^{\infty}\eta_j W_j(X) \tag{29}$$

where $W_j(X)$ is the j^{th} mode of buckling and η_j is the related constant. The latter constant represents the contribution of the jth mode of buckling in the deformed shape of the bimorph. The buckling modes are calculated to satisfy the boundary conditions as clarified in [23–25]. For clamped-clamped bimorphs, the following buckling modes can be considered:

$$\begin{array}{ll} W_j(X)=1-\cos N_jX & j=1,3,5,.. \\ W_j(X)=1-\cos N_jX-2X+\frac{2}{N_j}\sin N_jX & j=2,4,6,.. \end{array} \tag{30}$$

where N_j is the jth positive non-zero solution for the following equation:

$$\sin\frac{N_j}{2}\left(\tan\frac{N_j}{2}-\frac{N_j}{2}\right)=0. \tag{31}$$

The solutions of the later equation are obtained as follows:

$$\begin{array}{ll} N_j=(j+1)\,\pi & j=1,3,5,.. \\ N_j=2.86\pi,4.92\pi,6.94\pi,.. & j=2,4,6,... \end{array} \tag{32}$$

The modes of buckling are divided into symmetrical (modes 1, 3, 5, …) and unsymmetrical modes (modes 2, 4, 6, …). The first five modes of buckling are shown in figure 4.

As the bimorph deformation and loading conditions are symmetric relatively to the bimorph mid-length, the non-symmetrical modes of buckling (modes 2,4,6,…) are not involved in the solution, except for mode 2 which appears in a specific condition that will be clarified later.

$$W(X)=\sum_{j=1,3,5,\ldots}\eta_j W_j(X). \tag{33}$$

The solution is obtained by introducing (33) into (27) and calculating the constants η_j.

$$W(X)=\sum_{j=1,3,5,\ldots}\frac{\kappa_j}{N_j^2\left(N_j^2-N^2\right)}W_j(X). \tag{34}$$

The solution in (34) requires determining the normalized axial force N. Considering the normalized parameters in (28), the following equation for determining N is obtained by introducing (34) into (15), (16), (17), and (18).

$$\begin{aligned} N^2=&N_r^2+\frac{P_h l^2}{R_f}-\frac{4R_a l^4}{R_f^3}\cdot \\ &\left(\begin{array}{l} m^2S_1 \\ +2m\sum\limits_{n=1,3,5,\ldots} n\pi\, m_n S_{2n} \\ +\sum\limits_{n=1,3,5,\ldots} n^2\pi^2 m_n^2 S_{3n} \\ +2\sum\limits_{n=1,3,5,\ldots}\sum\limits_{h=3,5,7,\ldots}^{h>n} nh\pi^2 m_n m_h S_{4nh} \end{array}\right) \end{aligned} \tag{35}$$

where N_r is the normalized axial force due to residual stresses:

$$N_r^2=\frac{R_a l^2}{R_f}\varepsilon_r. \tag{36}$$

Once N is calculated by solving (35), the deflection of the bimorph at any point along its length can be obtained from (33). The deflection d of the bimorph at its mid-length ($x=l/2$) is considered as the main output parameter for the bimorph and is calculated from (33).

$$\begin{aligned} d=W\left(\frac{1}{2}\right)=&2\sum_{j=1,5,9,\ldots}\frac{\kappa_j}{N_j^2\left(N_j^2-N^2\right)} \\ =&\frac{8l^2}{R_f}\left(mS_5+\sum_{n=1,3,5,\ldots}n\pi\, m_n S_{6n}\right). \end{aligned} \tag{37}$$

The N equation (35) and d equation (37) contain infinite sums of first, double, and triple order series. Among these sums, S_1, S_{2n}, S_{3n}, S_{4nh}, S_5 and S_{6n} are infinite sums of series depending on N and N_j.

$$\begin{cases} S_1 = \displaystyle\sum_{j=1,3,5,\ldots} \frac{1}{N_j^2\left(N_j^2-N^2\right)^2} \\ S_{2n} = \displaystyle\sum_{j=1,3,5,\ldots} \frac{1}{\left(N_j^2-N^2\right)^2\left(N_j^2-n^2\pi^2\right)} \\ S_{3n} = \displaystyle\sum_{j=1,3,5,\ldots} \frac{N_j^2}{\left(N_j^2-N^2\right)^2\left(N_j^2-n^2\pi^2\right)^2} \\ S_{4nh} = \displaystyle\sum_{j=1,3,5,\ldots} \frac{N_j^2}{\left(N_j^2-N^2\right)^2\left(N_j^2-n^2\pi^2\right)\left(N_j^2-h^2\pi^2\right)} \\ S_5 = \displaystyle\sum_{j=1,5,9,\ldots} \frac{1}{N_j^2\left(N_j^2-N^2\right)} \\ S_{6n} = \displaystyle\sum_{j=1,5,9,\ldots} \frac{1}{\left(N_j^2-N^2\right)\left(N_j^2-n^2\pi^2\right)}. \end{cases} \tag{38}$$

Explicit analytical expressions can be extracted for the infinite sums S_1, S_{2n}, S_{3n}, S_{4nh}, S_5 and S_{6n}. These expressions are calculated using Mathematica software.

$$\begin{cases} S_1 = \dfrac{2N^2+3N^2\csc^2\frac{N}{2}+18N\cot\frac{N}{2}-48}{48N^6} \\ S_{2n} = \dfrac{1}{2n^2\pi^2N^4}+\dfrac{\csc^2\frac{N}{2}}{16N^2\left(N^2-n^2\pi^2\right)} \\ \qquad + \dfrac{\cot\frac{N}{2}\left(3N^2-n^2\pi^2\right)}{8N^3\left(N^2-n^2\pi^2\right)^2} \\ S_{3n} = \dfrac{\cot\frac{N}{2}\left(3N^2+n^2\pi^2\right)}{8N\left(N^2-n^2\pi^2\right)^3}+\dfrac{1+\csc^2\left(\frac{N}{2}\right)}{16\left(N^2-n^2\pi^2\right)^2} \\ S_{4nh} = \dfrac{\csc^2\frac{N}{2}}{16\left(N^2-n^2\pi^2\right)\left(N^2-h^2\pi^2\right)} \\ \qquad + \dfrac{\cot\frac{N}{2}\left(3N^4-\left(n^2+h^2\right)\pi^2N^2-n^2h^2\pi^4\right)}{8N\left(N^2-n^2\pi^2\right)^2\left(N^2-h^2\pi^2\right)^2} \\ S_5 = \dfrac{4\tan\frac{N}{4}-N}{32N^3} \\ S_{6n} = \dfrac{n\pi\tan\frac{N}{4}-N\tan\frac{n\pi}{4}}{8n\pi N\left(N^2-n^2\pi^2\right)}. \end{cases} \tag{39}$$

The sums S_1, S_{2n}, S_{3n}, S_{4nh}, S_5, and S_{6n} increase or decrease monotonically relatively to N until reaching $\pm\infty$ for $N=2\pi$. The value of these sums at $N=0$ and $N=\pi$ requires a limit calculus evaluation as certain denominators become equal to zero. These limits are calculated in table 1. Note that the structural model equations are derived considering an axial compression force, and thus a positive value for P. The resultant axial force can become tensile ($P<0$), especially when the bimorph undergoes large lateral deformation ($\varepsilon_d \gg 0$) or when residual strain leads to length contraction ($\varepsilon_r < 0$). The same equations apply in the case of axial tension, although N becomes an imaginary number. To remove the imaginary number from governing equations, N can be replaced by N_t in the equations, where $N_t^2 = -N^2 = -\frac{PL^2}{R_f}$, allowing the imaginary numbers to cancel out. Note that the trigonometric functions (e.g. sin, cos, tan) for imaginary numbers are equivalent to the hyperbolic functions for real number multiplied by an imaginary number. The same type of calculation was considered in [12] to derive the governing equations for the buckling of the single-material shallow beam actuators under tension.

Table 1. Values of S_1, S_{2n}, S_{3n}, S_{4nh}, S_5, and S_{6n} at $N=0$ and $N=\pi$.

		π	
N	0	$n=1$	$n>1$
S_1	$\frac{1}{60480}$		$\frac{5\pi^2-48}{48\pi^6}$
S_{2n}	$\frac{720-n^4\pi^4-60n^2\pi^2}{1440n^6\pi^6}$	$\frac{32-3\pi^2}{64\pi^6}$	$\frac{n^2\pi^2+8\left(n^2-1\right)}{16n^2(n^2-1)\pi^6}$
S_{3n}	$\frac{5n^2\pi^2-48}{48n^6\pi^6}$	$\frac{\pi^2-6}{768\pi^4}$	$\frac{1}{8(n^2-1)^2\pi^4}$
S_{4nh}	$\frac{n^2h^2\pi^2-12\left(n^2+h^2\right)}{24n^4h^4\pi^6}$	$\frac{-h^2-3}{64(h^2-1)^2\pi^4}$	$\frac{1}{16\pi^4(n^2-1)(h^2-1)}$
S_5	$\frac{1}{1536}$		$\frac{4-\pi}{32\pi^3}$
S_{6n}	$\frac{4\tan\frac{n\pi}{4}-n\pi}{32n^3\pi^3}$	$\frac{\pi-2}{32\pi^3}$	$\frac{-n+\tan\frac{n\pi}{4}}{8n\pi^3(n^2-1)}$

4. Behavior of the Electrothermal Bimorph

While the residual and electrothermal stresses are externally excited, the axial and bending stresses are internally induced due to the deformation of the bimorph. Increasing the external stresses, either through residual stresses (e.g. increasing N_r) or by electroheating (e.g. increasing Δv), would increases the axial force along the bimorph. The axial force, normalized by N, plays a key role in determining the behavior and direction of deflection of the bimorph.

First, without electrothermal heating, the bimorph is prestressed with the residual stresses which increases N. The latter has a critical limit at $N=N_1$ that it can reach but not exceed without electrothermal heating. At this limit, buckling occurs, resulting in two possible configurations: buckling upward or downward. Second, with electrothermal heating, N varies below or above $N=N_1$. Each range corresponds to deflection on the lower or upper side of buckling. This behavior of the bimorph is thoroughly explained in this section.

4.1. Bifurcation at first mode of buckling

The first motivation for this study was the use of bimorph buckling for an optical tuning application. However, during the microfabrication process, the bimorph structures consistently buckled after being released from the underlying substrate. This behavior indicated the presence of residual stresses. Despite numerous fabrication trials involving various parameters, we were unable to successfully reduce the residual stresses

to prevent buckling in the fabrication process for our bimorphs of specific dimensions and materials.

A significant challenge for the application is ensuring that all bimorphs buckle in the same direction. Consistent directionality is essential for controlling the individual relative phase delay, particularly when the top side of the bimorph is used for reflection. If some beams buckle upward while neighboring beams buckle downward, controlling the phase delay becomes complicated. Note that heating the bimorph after buckling increases the deflection in the same direction as the initial buckling. Hence, once buckled, there is no simple mechanism to re-buckle the bimorph towards the other side, especially in the case of mass distribution of bimorphs.

Understanding this buckling phenomenon prompted us to include the residual stresses into the calculation and derive the variation for the deformation energy with respect to the parameters of the solution to determine the conditions of buckling. The derivation of the energy variation equation closely resemble the case of a clamped-clamped beam made of a single material, as described in [23–25]. The energy variation equation for the bimorph is calculated as follows:

$$\partial U_t = \sum_{j=1}^{\infty} \left(2N_j^2 \left(N_j^2 - N^2\right) \eta_j\right) \partial \eta_j \tag{40}$$

where U_t is the normalized total energy. It's important to note that (40) is calculated without considering the electrothermal heating of the structure.

The parameters to be determined from (40) are the constants η_j representing the contribution of the modes of buckling in the total solution (33). The energy variation in (40) should be minimized, and it cannot be negative according to the variational principle. In the absence of residual or heating stresses, N is equal to zero. Adding residual stresses increases N_r, and $N = N_\mathrm{r}$ in the absence of heating stresses according to (35). This remains valid as long as $N_\mathrm{r} < N_1 = 2\pi$. In this range, $(N_j^2 - N^2)$ remains positive and non-negligible for all modes of buckling. Thus, the buckling constants η_j should be equal to zero for all modes of buckling to minimize ∂U_t (40).

This indicates that the bimorph remains straight without buckling during fabrication as long as the residual stresses are in the range $N_\mathrm{r} < N_1$. Once N_r reaches N_1 and exceeds it, N cannot exceed N_1 as this leads to a negative variation of energy (40), breaking the laws of nature. One could argue that allowing N to exceed N_1 while keeping η_1 equal to zero would minimize the energy variation. This is mathematically correct, but physically results in an unstable configuration for the bimorph where a minimum disturbance would move the bimorph far towards one of the two stable configurations at the two sides of buckling. The stable and unstable configurations for the bimorphs in the cases $N < N_1$ and $N > N_1$ are shown in figure 5, demonstrating typical curves for the variation of the deformation energy with the amplitude of η_1.

The first mode of buckling would increase the energy of deformation for $N < N_1$, while a specific magnitude of the first mode of buckling can minimize the energy of deformation for $N > N_1$, according to figure 5. Thus, at the critical limit of

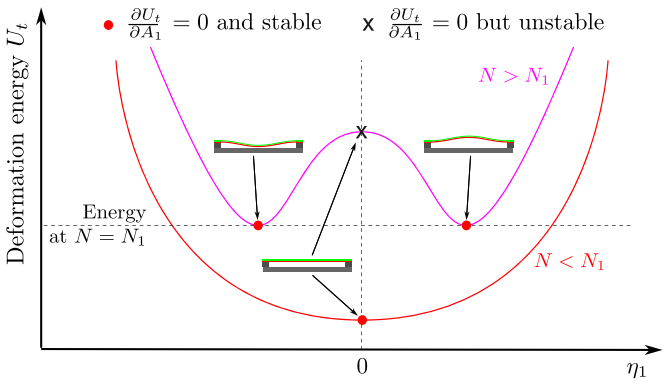

Figure 5. Variation of the deformation energy with the amplitude of the first mode of buckling (represented by η_1) for $N < N_1$ and $N > N_1$.

$N = N_1$, the bimorph buckles up or down to limit the energy of deformation. A bifurcation of the solution occurs at this critical limit of N, indicating a qualitative change in the behavior. Three possible solutions bifurcate, two of which are stable while the third is unstable. This indicates that the bimorph remains straight without buckling during fabrication as long as the residual stresses are in the range $N_\mathrm{r} < N_1$. Once N_r exceeds N_1, N remains limited at N_1 and buckling at first mode occurs in two possible directions.

$$\begin{cases} N = N_r & N_r < N_1 \& \Delta v = 0 \\ N = N_1 & N_r \geqslant N_1 \& \Delta v = 0 \end{cases}. \tag{41}$$

The constant η_1 is not necessarily equal to zero for $N_\mathrm{r} \geqslant N_1$. In this range, the bimorph takes the shape of the first mode of buckling while the value of N remains equal to N_1.

$$\begin{cases} W(X) = 0 & N_r < N_1 \& \Delta v = 0 \\ W(X) = \eta_1 W_1(X) & N_r \geqslant N_1 \& \Delta v = 0. \end{cases} \tag{42}$$

The normalized axial force equation is calculated by substituting (42) into (15) after normalization according to (28):

$$N^2 = N_r^2 - \frac{R_a}{4R_f} \eta_1^2 N_1^2. \tag{43}$$

The constant η_1, representing the contribution of the first mode of buckling, is calculated from (43) to keep $N = N_1$.

$$\eta_1 = \pm \sqrt{\frac{4R_f}{R_a} \left(\frac{N_r^2}{N_1^2} - 1\right)}. \tag{44}$$

The calculation in (44) shows two possible solutions for η_1 and thus two possible configurations with equal amplitude: buckling upward and downward. Figure 6 shows the variation of N and the amplitude of buckling depending on the normalized residual stress N_r.

The chances to buckle up or down are equal for a perfect structure and in the absence of external excitation. It is the

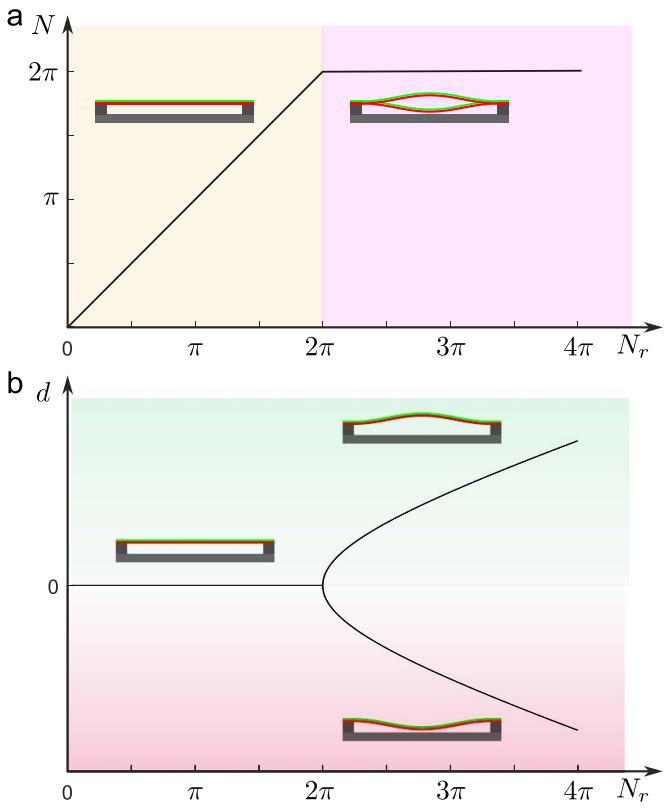

Figure 6. (a) Normalized axial force N as a function of normalized residual stress N_r. The first buckling mode emerges when N_r reaches N_1. (b) Variation of buckling amplitude with N_r. Buckling can occur in either of two directions when N_r exceeds N_1.

imperfections in the structure or the presence of external disturbance forces during the fabrication that lead to buckling up or down. In our fabrication process, we believe that the cohesion and attraction forces that appear during the release phase between the bimorph and the substrate led to buckling downward for the majority of the fabricated bimorphs. Furthermore, since the temperature of materials deposited to form the bimorphs is unknown (due to the absence of measurement capabilities in deposition tools), the residual stress cannot be estimated from the initial temperature of the bimorph layer and the thermal expansion mismatch during cooling. However, the residual strains can be estimated based on the amplitude of buckling observed after fabrication.

4.2. Electroheating before buckling at first mode

While the residual stresses depend on the fabrication process, the electrothermal heating is a controllable parameter that can be varied to control the deflection amplitude. As explained in the previous section, the electrothermal heating induces two types of loading along the bimorph length: axial force P_h and moment M_h. Both P_h and M_h are proportional to the square of the electric input (i.e. $\propto \Delta v^2$).

Before buckling at the first mode ($N_\mathrm{r} < N_1$), the direction of the heating moment is the main parameter that determines the direction of deflection for the bimorph. Although there are contributions from the 5$^{\mathrm{th}}$, 9$^{\mathrm{th}}$, 13$^{\mathrm{th}}$, … buckling modes, the first mode of buckling is dominant in the shape of the beam after deflection (37). Thus, the bimorph will be deflected upward or downward depending on the sign of κ_1 according to (37). Note that M_h along the beam and κ_1 should have the same sign in practice.

Table 2. Dimensions and material properties for a bimorph made of Silicon and Aluminium layers.

				Unit
l	200	b	1	μm
t_1	0.46	t_2	0.5	μm
E_1	70	E_2	179	*GPa*
ρ_1	$28.2 \cdot 10^{-9}$	ρ_2	0.1	$\Omega \cdot$ m
K_1	237	K_2	150	$\mathrm{W \cdot m^{-1} \cdot K^{-1}}$
α_1	23.6	α_2	3	$\mu m \cdot \mathrm{m^{-1} \cdot K^{-1}}$

$$\begin{cases} d > 0 & N_\mathrm{r} < N_1,\ \Delta v > 0, \& \kappa_1 > 0 \\ d < 0 & N_\mathrm{r} < N_1,\ \Delta v > 0, \& \kappa_1 < 0 \end{cases}. \tag{45}$$

Considering the bimorph dimensions and material properties in the example of table 2, M_h and κ_1 are positive, and thus the bimorph tends to deflect upward by increasing Δv.

Figure 7 shows the deflection of the bimorph and the variation of N in response to Δv for various values of N_r below N_1. The deflection direction is upward, as can be seen in these cases, and the deflection amplitude increases with Δv. The amplitude of the residual stress has a limited effect on the deflection amplitude. The axial force increases when Δv starts to increase as the bimorph length expands, and then starts to decrease at higher levels of Δv as the deflection becomes higher, which relaxes the axial force.

4.3. Electroheating after buckling at first mode

With electrothermal heating alone, the axial force N is not capable of reaching the critical limit for the first mode of buckling N_1, as can be seen in figure 7. However, buckling in the first mode can occur when the residual stresses ($\propto N_\mathrm{r}$) exceed a critical limit (i.e. $N_\mathrm{r} > N_1$), as can be seen in figure 6(a). In that case, the bimorph would have two stable configurations (buckling up and buckling down) as depicted in figure 6(b). The deflection amplitude would increase with the electrical input as in the previous case. However, the direction of deflection after electroheating is mainly similar to the initial direction of buckling induced by residual stresses.

Once the beam is buckled in the first mode, it has one of two stable configurations on either side of buckling. Electrothermal heating in any of these configurations induces two types of loading as usual: axial force P_h and moment M_h. It turns out that increasing the axial force P_h tends to amplify the buckling amplitude in the same direction as the initial buckling, while the heating moment tends to deflect the bimorph towards one direction regardless of the initial direction of buckling. Considering the bimorph example in table 2, M_h always pushes the bimorph up, while the axial force pushes

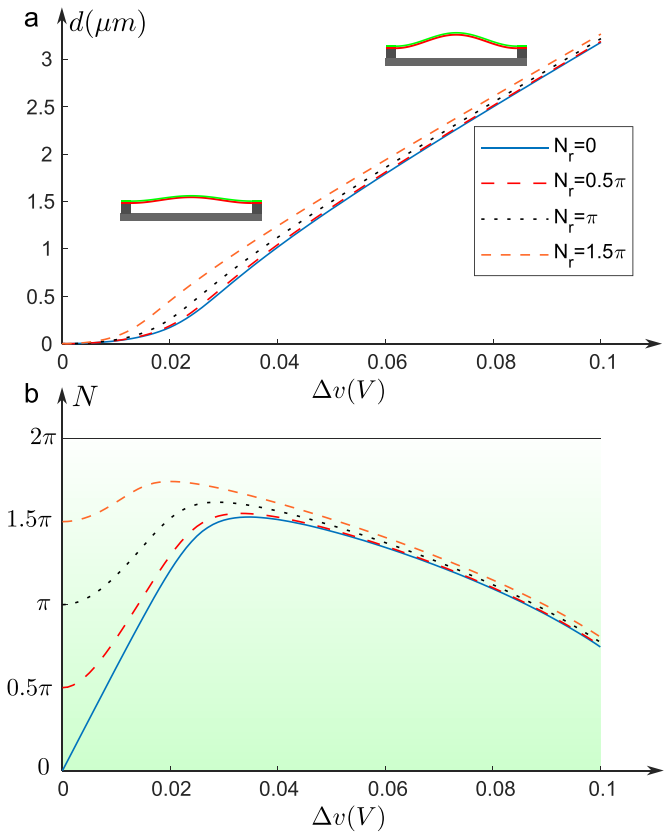

Figure 7. (a) Mid-length deflection of the bimorph d in response to the applied potential difference Δv for various values of N_r below N_1. (b) Variation of N with Δv for different values of N_r below N_1.

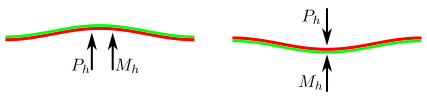

Figure 8. Effect of the heating axial force and moment on the deflection of the bimorph.

upward or downward when the bimorph is buckled up or down, respectively, as depicted in figure 8.

Figure 9 shows typical deflection and axial force variation for the bimorph as Δv increases starting from both sides of buckling. The curves show a slightly larger increase in the amplitude of the deflection in the buckled-up configuration due to the collaborative effect of P_h and M_h in this side of buckling, as depicted in figure 8.

Figure 9(b) shows two different ranges for the axial force N between the upper and lower configurations of the bimorph. N is below N_1 when the bimorph is buckled up and is above N_1 when it is buckled down.

The behavior of the buckled-up configuration is quite similar to the case of $N_r < N_1$. The differences are that, in the case of $N_r > N_1$, the deflection starts from a buckled configuration $d > 0$ (not from $d = 0$), and the normal force N only decreases with Δv, as N is initially at the maximum level for buckled-up configurations. figure 10 compares the deflection and axial force curves for buckled-up configurations at different levels of N_r.

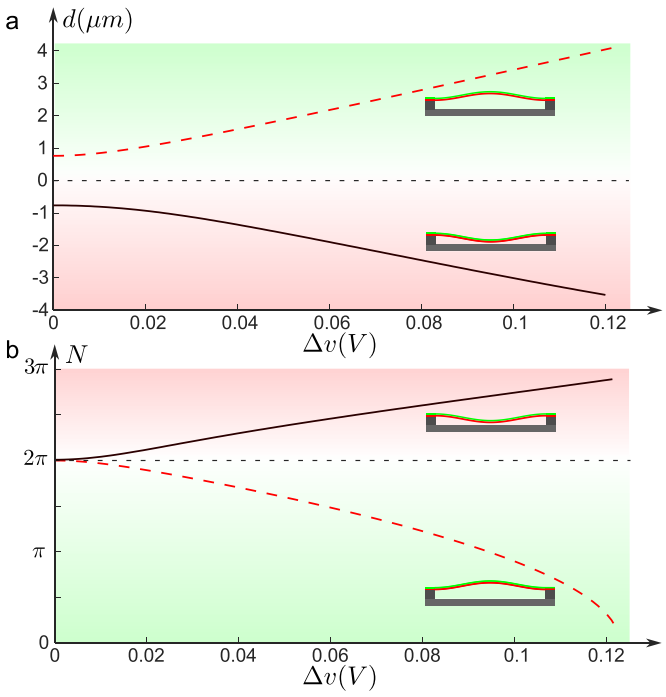

Figure 9. (a) Deflection of the bimorph d in response to Δv when N_r exceeds N_1 ($N_r = 2.5\pi$) and on both sides of buckling. (b) Variation of N with Δv on both sides of buckling.

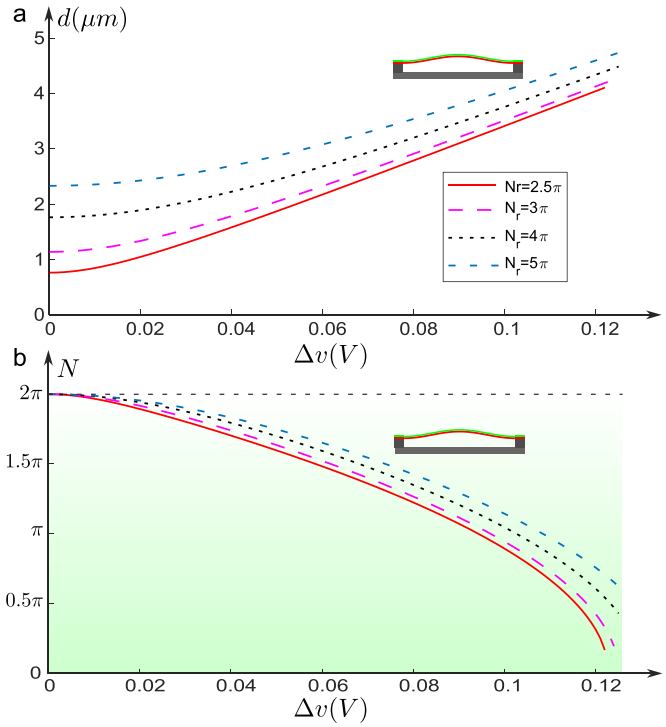

Figure 10. (a) Deflection of the bimorph d in response to Δv when N_r exceeds N_1 at different levels and the bimorph is on the upper side of buckling. (b) Variation of N with Δv for the different values of N_r.

The comparison in figure 10 shows that for larger values of N_r, there is a larger deflection and lower values of the axial force, likely due to the larger deflection. However, the

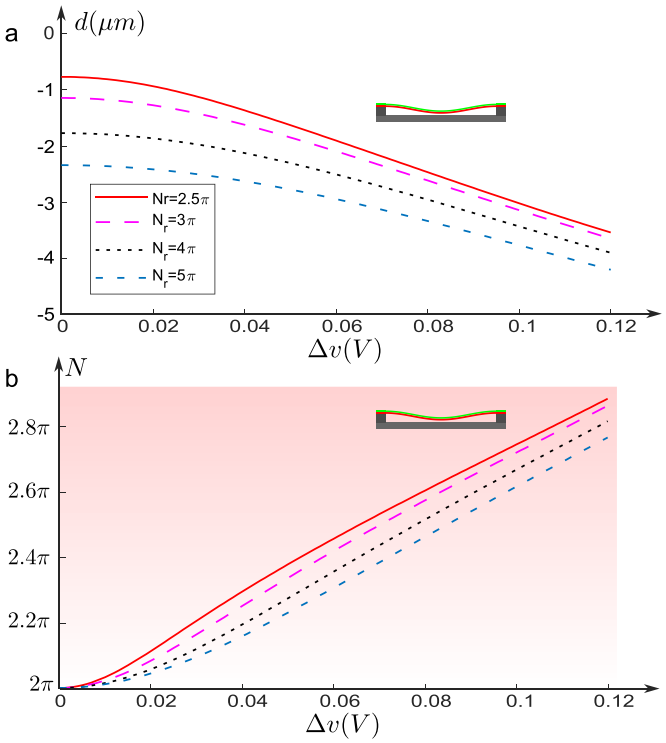

Figure 11. (a) Deflection of the bimorph d in response to Δv when $N_{\rm r}$ exceeds N_1 at different levels and the bimorph is on the bottom side of buckling. (b) Variation of N with Δv for the different values of $N_{\rm r}$.

difference between the deflection at its initial level before electroheating and after is higher for lower values of the residual stress.

Figure 11 compares the deflection and axial force curves for buckled-down configurations at different levels of $N_{\rm r}$. Similarly to the buckled-up configurations, a larger deflection and lower axial force occur in the buckled-down configurations for higher values of $N_{\rm r}$. However, the difference between deflection before and after electroheating is larger for lower values of $N_{\rm r}$.

The axial force in the buckled-down configurations increases due to the fact that the heating moment is pushing towards the other side of buckling which makes the bimorph length more compressed between the two fixed boundaries. The axial force N in this setting keeps increasing with Δv.

One can expect another bifurcation of solution once N reaches N_2, similar to the case of a clamped-clamped beam with a lateral force applied at the mid-length [23]. The second mode of buckling would appear in that case in the shape of the bimorph. However, we could not obtain such configurations in the FE simulations made on Ansys. Probably the reason is that the external moment due to heating is symmetrically applied along the bimorph with respect to the mid-length which prevent unsymmetrical deformation as unsymmetrical modes of buckling from occurring.

5. Numerical procedure and FE simulations

5.1. Numerical procedure

The analytical solutions derived in the previous sections for the temperature and deflection of an electrothermal bimorph can be calculated numerically in the following order for a specific bimorph with known materials and dimensions.

- Calculate z_0 (13), I_1, and I_2 (21).

Case 1: No electroheating is applied:

- Determine N according to (41).
- Calculate the bimorph deflection from (42) and (43).

Case 2: Electroheating is applied:

(a) Electrothermal model

- Calculate γ, β_n, a_{1n}, b_{1n}, a_{2n}, b_{2n}, a_{1n}, a_{1n} for $n = 1,3,5,\ldots$ up to a limited number of n (8).
- Calculate the temperature across the bimorph (4).

(b) Structural model

- Calculate P_h (18).
- Calculate m, m_{1n}, m_{2n}, and m_n (23).
- Calculate N by solving (35) and considering the infinite sums expressions in (39).
- Calculate κ_j (28) for $j = 1,3,5,\ldots$ up to a limited number of buckling modes j.
- Calculate the deflection along the bimorph (34).
- Calculate the deflection d at the mid-length (37) considering the infinite sums expressions in (39).

Once the solution is obtained, the strain at any point across the bimorph can be calculated using (9)–(12), and (14). The stress is then simply determined using Hooke's law.

Note that the solution of N with electroheating (35) might lie in different ranges, $N \in [0, N_1]$, $N^2 < 0$, and $N > N_1$. The solution with deflection direction same as the direction driven by the heating moment M_h would have $N < N_1$, while the solution with deflection in the opposite direction would have $N > N_1$. It is important to look for the solution of N in the corresponding ranges when solving (35). At large deflection, the axial force might reduce to become negative, moving from axial compression to tension. With negative axial force P, N becomes an imaginary number with $N^2 < 0$. In this case, the same governing equations still apply as the imaginary number would cancel out in all the expressions that are dependent on N.

As for the number of heating and buckling modes to be considered, it depends on the level of accuracy required in the solution. In our calculation, we consider 101 heating modes

and 201 buckling modes, which resulted in a very good agreement with FE simulations. For simplification, one can consider very few modes in the calculation as the effect of higher-order modes on the solution significantly decreases from one mode to the other.

Other electrothermal models, whether simpler, more advanced, or dynamic, can be considered for calculating the temperature. The coupling between the electrothermal and structural models is established through the thermal expansion relationship given in (11). Once the temperature is obtained from the electrothermal model, the thermal strain is calculated is calculated using (11), and the corresponding thermal force and moment are derived from (18) and (22), respectively. The same steps can then be followed to solve the structural model.

5.2. FE simulations

We noticed a perfect agreement in the comparison between the analytical models provided in this paper and the FE simulations run in ANSYS, both at the level of the electrothermal model and the structural model under different conditions.

The Ansys simulations use a structural-thermoelectric tetrahedron element (Plane223) with a fine planar mesh to couple thermoelectric effects with heat conduction and mechanical equilibrium equations, accounting for thermal expansion. The FE simulations were conducted using the same dimensions and material properties listed in table 2. Mesh points are added along the neutral line (with height levels calculated according to (13)) to compare the deflection with the analytical model. Fixed displacement and a constant temperature at $T_0 = 25°C$ are applied as boundary constraints on the bimorph ands. The bimorph is pre-strained with residual strains calculated according to (36) ($\varepsilon_r = R_f N_r^2/(R_A l^2)$). A voltage difference is then applied between the two fixed boundaries of the bimorph.

Figure 12 shows three comparisons between the mid-length deflection of the bimorph with electroheating, calculated analytically and obtained from FE simulations.

The comparisons in figure 12 consider three different initial conditions: residual stresses $N_r = 1.5\pi < N_1$ (figure 12(a)), and residual stresses $N_r = 2.5\pi > N_1$ with initial buckled-up (figure 12(b)) and buckled-down (figure 12(c)) configurations. The comparisons in all cases show a perfect correspondence to the extent that it is difficult to differentiate between the curves of the analytical model and FE simulations in the figure. For the initially buckled configurations, the direction of buckling was controlled in the simulation by forcing a mid-length deflection of the bimorph in a specific direction before releasing the deflection constraint and applying electroheating.

Note that each point in the simulation curves corresponds to a separate simulation run. To demonstrate the agreement between the calculated temperature and deflection across the bimorph, we select the simulation run corresponding to $N_r = 1.5\pi$ and $\Delta v = 0.12$ V. In those conditions, figure 13 shows the deflected shape of the bimorph with the temperature distribution across the bimorph obtained from both the analytical models and FE simulation.

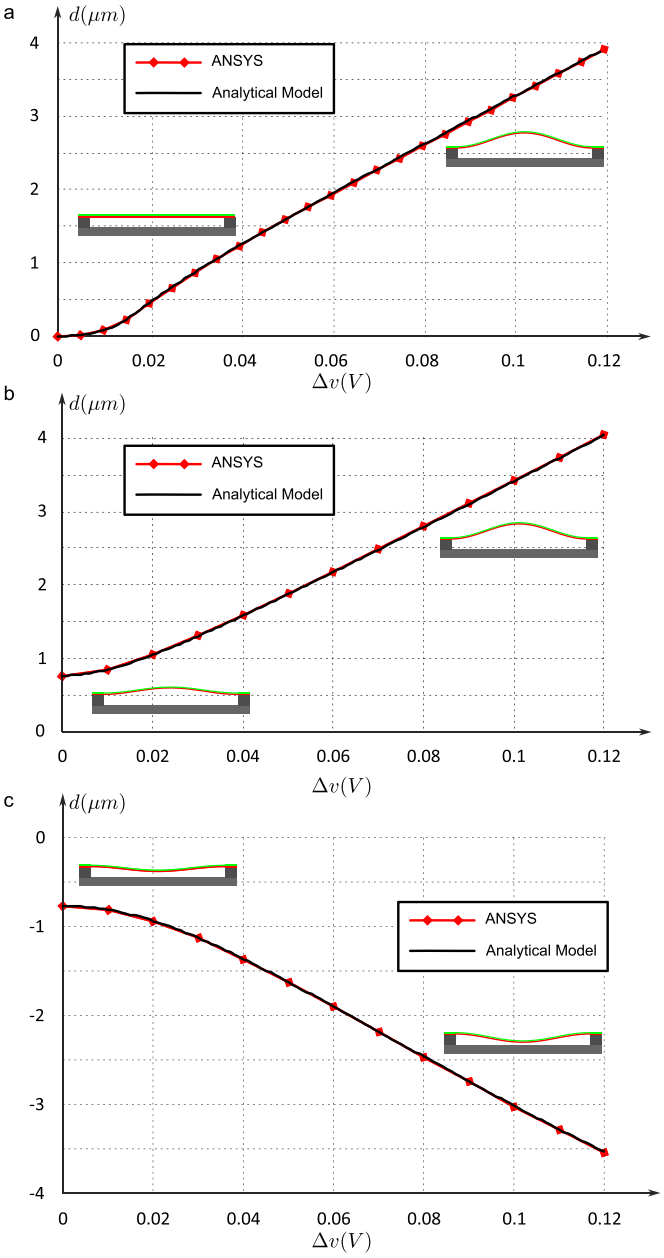

Figure 12. Comparison of mid-length deflection of the bimorph with electroheating: (a) residual stresses $N_r = 1.5\pi < N_1$, (b) residual stresses $N_r = 2.5\pi > N_1$ with initial buckled-up configuration, and (c) residual stresses $N_r = 2.5\pi > N_1$ with initial buckled-down configuration.

As it is difficult to notice differences in the two separate drawings in figure 13, and to better clarify the agreement, figure 14 shows a combined comparison between the analytical models and FE simulations for the average temperature and the deflection profile of the bimorph.

Each point in the average temperature curve represents the average temperature in the cross-section at the corresponding position along the bimorph. The deflected profile represents the deflection of the neutral line. The level of agreement

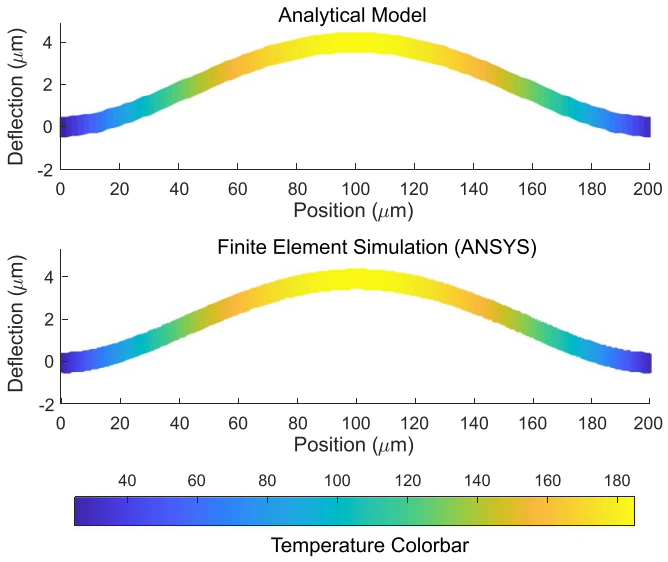

Figure 13. Comparison between deflected shape of the bimorph and internal temperature distribution calculated with both the analytical models developed in this paper and FE simulations performed in ANSYS. Residual stresses corresponding to $N_r = 1.5\pi$ and a potential difference $\Delta v = 0.12$ V are applied to the bimorph.

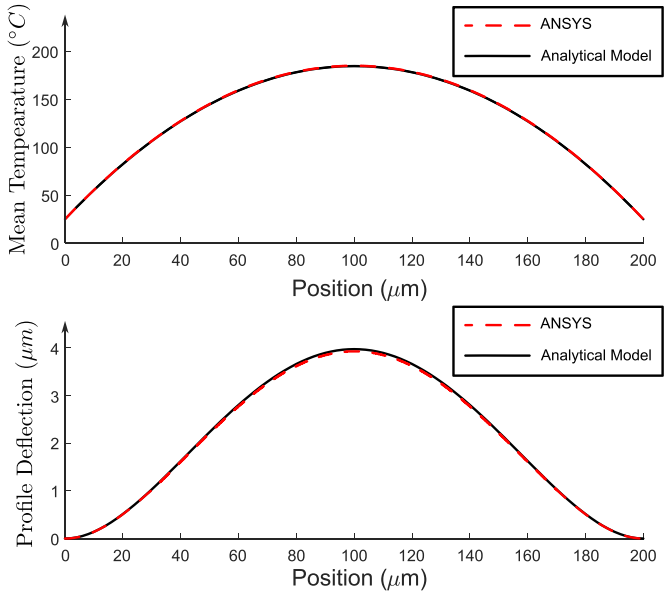

Figure 14. Comparison between the analytical model and FE simulation results for (a) the average temperature and (b) the deflection profile of an electrothermal bimorph. The bimorph is subjected to residual stresses corresponding to $N_r = 1.5\pi$ and a potential difference of $\Delta v = 0.12$ V.

between both the temperature and deflection results is quite excellent as is the case for the mid-length deflection comparisons shown in figure 13 which reveals the correctness and high accuracy of both the electrothermal and structural models developed in this paper.

6. Conclusion

This paper successfully developed and validated analytical electrothermal and structural models for electrothermal bimorphs. The electrothermal model provides a comprehensive understanding of the temperature distribution due to electrothermal heating, offering a 2D explicit analytical expression for temperature estimation along the bimorph's length and cross-section. This enables accurate calculation of thermal expansion and the resultant strains, forces, and moments.

The structural model effectively derives the governing equation for bimorph deflection, accounting for deformation, electrothermal heating, and residual stresses. By incorporating infinite sums of heating and buckling modes, the model presents a robust analytical solution for deflection, with closed-form equivalent expressions where feasible.

The analytical models were rigorously compared with FE simulations using Ansys, showing excellent agreement and confirming their high accuracy. These models elucidate the behavior of bimorphs under various scenarios of residual stresses and electrothermal heating, offering valuable insights for addressing fabrication challenges posed by residual stresses, and designing optimized bimorph-based optical devices.

Funding

This work was supported by OIA-2134345.

Data availability statement

All data that support the findings of this study are included within the article (and any supplementary files).

ORCID iDs

Hussein Hussein https://orcid.org/0000-0002-8417-3835
Quentin A A Tanguy https://orcid.org/0000-0002-2783-2881
Issam Lakkis https://orcid.org/0000-0002-6108-467X
Hossein Fariborzi https://orcid.org/0000-0002-7828-0239
Arka Majumdar https://orcid.org/0000-0003-0917-590X
Karl F Böhringer https://orcid.org/0000-0002-9428-2648

References

[1] Fang Z, Chen R, Zheng J and Majumdar A 2022 Non-volatile reconfigurable silicon photonics based on phase-change materials *IEEE J. Sel. Top. Quantum Electron.* **28** 1–17
[2] Zhang Z, Shi H, Wang L, Chen J, Chen X, Yi J, Zhang A and Liu H 2023 Recent advances in reconfigurable metasurfaces: principle and applications *Nanomaterials* **13** 534
[3] Gu T, Kim H J, Rivero-Baleine C and Hu J 2023 Reconfigurable metasurfaces towards commercial success *Nat. Photon.* **17** 48–58

[4] Tao H, Strikwerda A C, Fan K, Padilla W J, Zhang X and Averitt R D 2009 Reconfigurable terahertz metamaterials *Phys. Rev. Lett.* **103** 147401

[5] Zhu W M *et al* 2011 Switchable magnetic metamaterials using micromachining processes *Adv. Mater.* **23** 1792–6

[6] Lin Y-S and Lee C 2014 Tuning characteristics of mirrorlike t-shape terahertz metamaterial using out-of-plane actuated cantilevers *Appl. Phys. Lett.* **104** 251914

[7] Liu X and Padilla W J 2017 Reconfigurable room temperature metamaterial infrared emitter *Optica* **4** 430-433

[8] Mao Y, Pan Y, Zhang W, Zhu R, Xu J and Wu W 2016 Multi-direction-tunable three-dimensional meta-atoms for reversible switching between midwave and long-wave infrared regimes *Nano Lett.* **16** 7025–9

[9] Ou J Y, Plum E, Zhang J and Zheludev N I 2013 An electromechanically reconfigurable plasmonic metamaterial operating in the near-infrared *Nat. Nanotechnol.* **8** 252–5

[10] Ou J Y, Plum E, Jiang L and Zheludev N I 2011 Reconfigurable photonic metamaterials *Nano. Lett.* **11** 2142–4

[11] Hussein H, Le Moal P, Bourbon G, Haddab Y and Lutz P 2015 Analysis of the dynamic behavior of a doped silicon U-shaped electrothermal actuator *2015 IEEE Int. Conf. on Advanced Intelligent Mechatronics (AIM)* vol 2015(IEEE) pp 836–41

[12] Hussein H, Fariborzi H and Younis M I 2020 Modeling of Beam Electrothermal Actuators *J. Microelectromech. Syst.* **29** 1–12

[13] Zhang C, Yin X, Chen R, Ju K, Hao Y, Wu T, Sun J, Yang H and Xu Y 2024 A review on reprogrammable bistable structures *Smart Mater. Struct.* **33** 093001

[14] Sawada R 2018 Optical switch *Encyclopedic Handbook of Integrated Optics* (CRC Press) pp 247–58

[15] Halg B 1990 On a micro-electro-mechanical nonvolatile memory cell *IEEE Trans. Electron Devices* **37** 2230–6

[16] Ratnayake D, Martin M D, Gowrishetty U R, Porter D A, Berfield T A, McNamara S P and Walsh K M 2015 Engineering stress in thin films for the field of bistable mems *J. Micromech. Microeng.* **25** 125025

[17] Xu R, Akay H and Kim S-G 2019 Buckled mems beams for energy harvesting from low frequency vibrations *Research* **2019**

[18] Hussein H, Bouhadda I, Mohand-Ousaid A, Bourbon G, Le Moal P, Haddab Y and Lutz P 2018 Design and fabrication of novel discrete actuators for microrobotic tasks *Sens. Actuators* A **271** 373–82

[19] Hussein H and Fariborzi H 2022 Accurate sensorless multistable microsystem with a single actuator *Front. Mech. Eng.* **8** 5

[20] Hussein H, Bazroun A A and Fariborzi H 2022 Microrobotic leg with expanded planar workspace *IEEE Robot. Autom. Lett.* **7** 5998–6004

[21] Hussein H, Damdam A, Ren L, Charrouf Y O, Challita J, Zwain M and Fariborzi H 2023 Actuation of mobile microbots: a review *Adv. Intell. Sys.* **5** 2300168

[22] Bloom D M 1997 Grating Light Valve: revolutionizing display technology Proc. SPIE **3013** 165–71

[23] Qiu J, Lang J H and Slocum A H 2004 A curved-beam bistable mechanism *J. Microelectromech. Syst.* **13** 137–46

[24] Hussein H, Le Moal P, Bourbon G, Haddab Y and Lutz P 2015 Modeling and stress analysis of a pre-shaped curved beam: influence of high modes of buckling *Int. J. Appl. Mech.* **07** 1550055

[25] Hussein H and Younis M I 2020 Analytical study of the snap-through and bistability of beams with arbitrarily initial shape *J. Mech. Robot.* **12** 1–21

[26] Giannopoulos G, Monreal J and Vantomme J 2007 Snap-through buckling behavior of piezoelectric bimorph beams: I. analytical andnumerical modeling *Smart Mater. Struct.* **16** 1148

[27] Hu K M, Li H and Wen L H 2020 Experimental study of axial-compressed macro-fiber composite bimorph with multi-layer parallel actuators for large deformation actuation *J. Intell. Mater. Syst. Struct.* **31** 1101–10

[28] Timoshenko S 1925 Analysis of bi-metal thermostats *JOSA* **11** 233–55

[29] Tai Y C, Mastrangelo C H and Muller R S 1988 Thermal conductivity of heavily doped low-pressure chemical vapor deposited polycrystalline silicon films *J. Appl. Phys.* **63** 1442–7

[30] Fedder G K and Howe R T 1991 Thermal assembly of polysilicon microstructures *Proc. IEEE Micro Electro Mechanical System Workshop* pp 63–68

[31] Lin L and Chiao M 1996 Electrothermal responses of lineshape microstructures *Sens. Actuators* A **55** 35–41

[32] Manginell R P, Smith J H, Ricco A J, Hughes R C, Moreno D J and Huber R J1997 Electrothermal modeling of a microbridge gas sensor *Proc. SPIE* **3224** 360–71

[33] Todd S T and Xie H 2005 Steady-state 1d electrothermal modeling of an electrothermal transducer *J. Micromech. Microeng.* **15** 2264–76

[34] Todd S T and Huikai X 2008 An electrothermomechanical lumped element model of an electrothermal bimorph actuator *J. Microelectromech. Syst.* **17** 213–25

[35] Bergman T L 2011 *Fundamentals of Heat and Mass Transfer* (Wiley)

[36] Dutta S and Pandey A 2021 Overview of residual stress in mems structures: its origin, measurement and control *J. Mater. Sci., Mater. Electron.* **32** 6705–41

[37] Pulskamp J S, Wickenden A, Polcawich R, Piekarski B, Dubey M and Smith G 2003 Mitigation of residual film stress deformation in multilayer microelectromechanical systems cantilever devices *J. Vac. Sci. Technol.* B **21** 2482–6